Development of a dual-mode electro-hydrostatic actuator with serial-parallel hybrid configured piezoelectric pumps

To cite this article: Jie Ling *et al* 2023 *Smart Mater. Struct.* **32** 025011

IOP Publishing Smart Materials and Structures
Smart Mater. Struct. **32** (2023) 025011 (17pp) https://doi.org/10.1088/1361-665X/acafb5

Development of a dual-mode electro-hydrostatic actuator with serial-parallel hybrid configured piezoelectric pumps

Jie Ling, Long Chen, Mingming Zhang and Yuchuan Zhu*

National Key Laboratory of Science and Technology on Helicopter Transmission, Nanjing University of Aeronautics and Astronautics, Nanjing 210016, People's Republic of China

E-mail: meeyczhu@nuaa.edu.cn

Received 23 September 2022, revised 17 November 2022
Accepted for publication 3 January 2023
Published 19 January 2023

Abstract

Smart materials-based electro-hydrostatic actuator (EHA) plays an important role in the power-by-wire technology for the next generation of more electric aircraft. However, the output flow of a smart materials-based EHA is relatively low to narrow down its practical applications. To address this issue, a piezoelectric material-based dual-mode electro-hydrostatic actuator (DMEHA) is proposed in this work. The output flow can be improved by adopting two piezoelectric pumps without sacrificing the carrying capacity. In addition, a hybrid serial and parallel configuration for the two pumps is realized for the adaptability of different actuation requirements. Mathematical modeling and parameter identification are conducted and presented in detail for the designers. A physical prototype is fabricated and a series of experiments are carried out to investigate its characteristics. Results indicated that the DMEHA achieves a maximum output flow of 1.17 l min^{-1} at 360 Hz under the serial mode and the blocking load up to 40 kg. The corresponding maximum output flow in the parallel mode can reach 1.96 l min^{-1} at 420 Hz, and the blocking load is 20 kg.

Keywords: piezoelectric pump, electro-hydrostatic actuator, dynamic modelling, dual-mode actuator

(Some figures may appear in colour only in the online journal)

1. Introduction

As the core technology of the next generation of more electric aircraft [1, 2], power-by-wire technology has been applied both in A380 in the civil aviation field and in F35 in the military field [3, 4]. However, power-by-wire systems have not yet replaced traditional hydraulic systems in aircraft, where they are equipped for backup uses. The main limiting factor is that the power-by-wire systems put forward a high requirement on the electro-hydrostatic actuator (EHA) [5–7]. Traditional EHAs powered by motor-driven hydraulic pumps with low energy density and low reliability are unable to meet the demands [8, 9]. Development of EHAs with light, integrated, high power-to-weight ratio and redundancy characteristics is urgent for the next generation of more electric aircraft [10, 11].

Smart materials-based EHAs [12–14] have shown a broad application prospect in the field of aviation owing to the merits of high energy density and high bandwidth [15, 16]. These EHAs are configured with smart materials-driven pumps coupled with hydraulic cylinders and pipelines. The high-frequency reciprocating micro-displacement movement of smart material actuators can be converted into the large displacement output of the hydraulic cylinder with high

* Author to whom any correspondence should be addressed.

power density [17]. The smart material actuator generates displacement under external excitation to push the piston to compress the oil, which is rectified through the valve and continuously enters the hydraulic cylinder to form continuous motion [18]. Herein, as an important index, the flow rate of the EHA depends on the stroke and operating frequency of the smart material actuator. Although the bandwidth of some smart material actuators can reach several thousand Hz [19, 20], the output displacement can only reach one to two thousandths of their length [21]. As a result, the output flow of EHA driven by smart materials is relatively low to meet the requirements of practical applications.

In order to improve the output flow of smart material-based EHAs, researchers have carried out some explorations. One way to increase the EHA flow is to increase the output displacement of the smart materials. Bartlett *et al* [22] proposed a lever displacement amplification mechanism for smart material actuators. Through the employment of a simple strain amplification lever mechanism, displacements between 0.5 mm and 4 mm were achieved with associated forces of between 6 kN and 0.5 kN, respectively. Qin *et al* [23] proposed a decoupled 2-DOF monolithic mechanism, in which statically indeterminate leaf parallelograms provide the decoupling effect, and the displacement of the piezoelectric actuator (PEA) is amplified with a statically indeterminate lever mechanism. Yang *et al* [24] proposed a hydraulic amplification mechanism for smart material actuators and the dynamic analysis of which indicated that the amplifier is amenable to enlarge the micro stroke of actuators in different driving current levels. Tian *et al* [25] developed a spatial deployable three-degree of freedom compliant nanopositioner with a three-stage flexible hinge motion amplification mechanism. Experimental results demonstrate that the maximum displacements in x, y, and z-axes can reach 177.33, 179.30, and 17.45 μm, respectively. Chen *et al* [26] proposed a multidimensional discrete configuration for the displacement amplification of magnetostrictive actuators, which has a displacement magnification of 3 times and does not sacrifice bandwidth. However, the adoption of the displacement amplification mechanism achieves larger output displacement at the expense of the output force. Consequently, increasing the flow rate of the EHA by amplifying the output displacement of the smart material will sacrifice its carrying capacity.

The resonant mode driving method of a piezoelectric pump is another way to increase the EHA flow. To improve the driving capacity of piezoelectric membrane pumps, a novel resonantly driven piezoelectric gas pump with annular bimorph as the driver is proposed by Wu *et al* [27]. And the experimental results indicate that 70 V of sinusoidal AC driving voltage, the improved pump amplified the piezoelectric vibrator displacement by 4.2 times, and the maximum gas output flow rate reached 1685 ml min^{-1}. Wang *et al* [28] proposed a compact resonant piezoelectric diaphragm pump with the employment of an elastic mass to adjust the system's resonance frequency. The experimental results show that the diaphragm system reaches resonance under the driving frequency of 265 Hz, the diaphragm's amplitude is double amplified and the maximum gas flow rate is achieved as 186.8 ml min^{-1}. A resonant type piezoelectric pump driven by a tuning fork vibrator is developed by Pan *et al* [29], and the resonant frequency of which is designed to be the power frequency, the maximum flow rate of which at the resonant frequency can reach 441.77 ml min^{-1}. In order to improve the output pressure of the piezoelectric pump, a resonant piezoelectric pump using a displacement-amplifying vibrator is proposed by Pan *et al* [30] in another study. The displacement-amplifying vibrator consists of two piezoelectric stacks with two amplifiers and works in the resonant state. The experimental results show that the proposed piezoelectric pump has a maximum output pressure up to 4.73 MPa, and a maximum flow rate of 65.7 ml min^{-1}. By adding a special mechanism to make the piezoelectric pump work at the resonant frequency, the displacement of the PEA and the volume change of the piezoelectric pump can be amplified effectively to improve the output flow. However, the current research on resonant amplification is mainly focused on piezoelectric membrane air pumps, the application of the resonance principle to liquid piezoelectric pump needs further research.

Another direct way to increase the EHA flow is to increase the number of pump cavities. Ullmann [31] analyzed the multi-pump combination form of the piezoelectric pump with increasing the number of pump cavities and compared the pump performance of each different combination form of pump cavities under the same driving mode. The results showed that the performance of double pumps in series was better. Kan *et al* [32] developed a piezoelectric pump with four pump cavities in series and analyzed the characteristics of piezoelectric pumps with single pump cavity, double pump cavity, three pump cavity, and four pump cavities at different frequencies. Experimental results show that the output flow of the piezoelectric pump can be effectively increased by the serial connection of four pump cavities. Dong *et al* [33] proposed a new kind of piezoelectric pump with triple cavities in series and the experimental results show that the maximum flow rate of the piezoelectric pump reached 1513.2 ml min^{-1} when the driving frequency was 220 Hz. Wang *et al* [34] proposed a new type of a dual magnetostrictive material rod-based EHA with the double pump parallel configuration. The peak flow is achieved as 2.6 l min^{-1} under no-load conditions, and the estimated maximum load can reach 55 kg. Zhu *et al* [35] proposed an EHA driven by dual axial-mounted magnetostrictive material rods-based pumps with the double pump parallel configuration and the experimental results indicate that the maximum flow rate can reach approximately 2.7 l min^{-1}, while the operating frequency is 180 Hz. Unfortunately, the multi-pump serial structure can increase the carrying capacity of the EHA exponentially, but the flow increase is limited. Correspondingly, the multi-pump parallel structure can effectively improve the flow rate but cannot adapt to the condition of a large load. Therefore, there is always a trade-off between large flow and large carrying capacity in the single-mode structure, i.e. either in the multi-pump serial structure alone or in

Table 1. The summary of properties for smart material-based pumps.

Studies	Type	Driver	Frequency	Pressure	Flow rate	Medium
Kan *et al* [32]	four pump in series	PM film	280 Hz	48.6 kPa	7.6 ml min^{-1}	Air
Wu *et al* [27]	single pump in resonant	PM film	230 Hz	N/A	1.68 l min^{-1}	Air
Wang *et al* [28]	single pump in resonant	PM film	265 Hz	56.7 kPa	0.19 l min^{-1}	Air
Dong *et al* [33]	triple pump in series	PM film	220 Hz	4.08 kPa	1.5 l min^{-1}	Air
Wang *et al* [34]	dual pump in parallel	MM stack	150 Hz	0.6 MPa	2.6 l min^{-1}	Oil
Pan *et al* [29]	single pump in resonant	PM film	50 Hz	N/A	0.44 l min^{-1}	Water
Pan *et al* [30]	single pump in resonant	PM stack	395 Hz	4.73 MPa	65.7 ml min^{-1}	Air
Zhu *et al* [35]	dual pump in parallel	MM stack	180 Hz	0.6 MPa	2.7 l min^{-1}	Oil

the multi-pump parallel structure alone. The properties of the smart material-based pumps mentioned above are summarized in table 1.

In this paper, a novel piezoelectric material-based dual-mode electro-hydrostatic actuator (DMEHA) is proposed. With the employment of hybrid serial and parallel configured piezoelectric pumps, the DMEHA can adjust its working mode according to the working conditions. In order to realize the switch between the serial and parallel working mode of the double pump cavity, a two-position four-way electromagnetic directional valve is integrated into the valve block to change the state between the four inlet and outlet ports of the double pumps. Mathematical modeling is conducted for each module unit of the developed DMEHA, including the piezoelectric stack pump module, cantilever valve module, pipeline module, solenoid valve module, and hydraulic cylinder module. The unknown parameters in the model were identified by finite element simulations and experiments. Finally, a prototype is fabricated and a series of experiments were carried out to investigate the characteristics of the proposed DMEHA. The characteristics of the developed DMEHA and the contribution of this work are twofold:

(a) A novel configuration with two piezoelectric pumps is developed, modeled, and analyzed to increase the EHA flow. This provides an alternative framework for designing smart material-based multi-pump EHAs.
(b) The serial-parallel hybrid working mode is realized by the DMEHA for the adaptability of different actuation requirements. This takes both the advantages of the multi-pump serial structure and the multi-pump parallel structure. Results indicated that the DMEHA has a maximum output flow of 1.17 l min^{-1} at 360 Hz under the serial mode and the blocking load up to 40 kg. The corresponding maximum output flow in the parallel mode can reach 1.96 l min^{-1} at 420 Hz, and the blocking load is 20 kg.

The rest of this paper is organized as follows. The structure and working principle of the proposed DMEHA are introduced in section 2. The mathematical modeling for each module unit of the DMEHA is carried out in section 3. In section 4, parameter identification and accuracy verification of the mathematical model are conducted. In section 5, a prototype of the proposed DMEHA is fabricated and a series of experiments are carried out. In section 6 some discussions are made. Finally, section 7 ends with some conclusions.

2. Structure and working principle

2.1. Structure of the dual pumps EHA

The structure of the proposed DMEHA is shown in figure 1. It mainly comprises two piezoelectric stack-based pumps, an integrated pump chamber, a series-parallel valve block, a solenoid-operated directional control valve (HYDRAFORCE, SV08-43), solenoid-operated proportional valve (HYDRAFORCE, SP08-47CL) and hydraulic cylinder. The piezoelectric stack pump is the power source of the DMEHA. The piezoelectric stack outputs high-frequency reciprocating motion, then pushes the plunger in the integrated pump chamber, and finally converts mechanical energy into hydraulic energy. The integrated pump chamber provides space for installing the discharge and suction diaphragm valves, which rectify the oil in one direction. The hydraulic cylinder is the actuating end of the DMEHA. The series-parallel valve block that integrates the solenoid-operated directional control valve and the solenoid-operated proportional valve is applied to connect the pump chamber and the hydraulic cylinder and to switch the DMEHA's operating mode.

There are two operating modes for the DMEHA: series mode and parallel mode, which can be switched by the solenoid-operated directional control valve. The corresponding relationship between the spool position and the working mode is shown in figure 2. The appropriate operating mode can be selected according to the load requirements.

2.1.1. Series mode. When the coil of the solenoid-operated directional control valve is not energized, the DMEHA is in series mode, as shown in figure 3(a). In the first half cycle, the oil is discharged by pump 2, flows through the valve, and is drawn in by pump 1. The output pressure of pump 2 is used as an initial build-up in the pump chamber of pump 1. In the second half cycle, pump 1 discharges the oil to the hydraulic cylinder, and pump 2 re-absorbs oil from the low-pressure side of the cylinder. Therefore, under the premise of neglecting piping losses and considering the output performance of two pumps to be identical, the load characteristic P_s and output flow characteristic Q_s of the DMEHA in series mode can be expressed as follows:

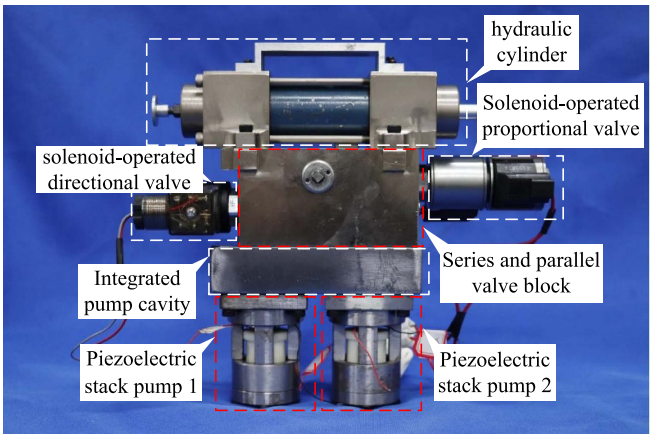

Figure 1. The structure of the DMEHA.

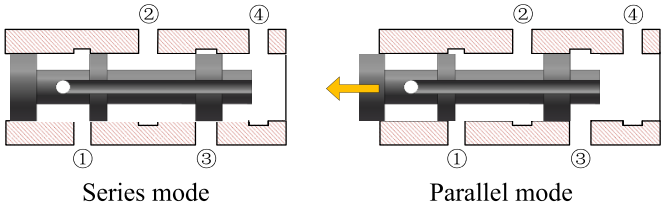

Figure 2. The different spool positions of the solenoid-operated directional control.

$$P_s = P_1 + P_2 = 2P_1 = 2P_2 \tag{1}$$

$$Q_s = C_v A\sqrt{\frac{2P}{\rho}} = C_v A\sqrt{\frac{2(P_1+P_2)}{\rho}} = \sqrt{2}Q_1 = \sqrt{2}Q_2 \tag{2}$$

where Q_1 and Q_2 are the output flow rates of piezoelectric stack pump 1 and pump 2, respectively, P_1 and P_2 are the output pressures of pump 1 and pump 2, respectively, and C_v, A and ρ represent the flow coefficient, through-flow area, and oil density, respectively.

2.1.2. Parallel mode. When the valve coil is energized, the DMEHA is in parallel mode, as shown in figure 3(b). In this case, the two pumps do not interfere with each other. In the first half cycle, pump 1 discharges oil to the hydraulic cylinder, and pump 2 draws oil from the hydraulic cylinder. In the second half cycle, pump 2 discharges oil to the hydraulic cylinder, and pump 1 draws oil from the hydraulic cylinder. In one cycle, pumps 1 and 2 perform one oil discharge. Therefore the output flow rate of the DMEHA is twice that of the single pump. But during the discharge of pump 1 and 2, the output pressure of each pump did not add up. The load characteristic P_p and output flow characteristic Q_p of the DMEHA in parallel mode can be expressed as:

$$P_p = P_1 = P_2 \tag{3}$$

$$Q_p = Q_1 + Q_2 = 2Q_1 = 2Q_2. \tag{4}$$

2.2. Working principle of the DMEHA

The solenoid-operated proportional valve can regulate the DMEHA's direction of motion. Taking the parallel mode as an example, pump 1 and pump 2 are driven by two voltage signals with a phase difference of 180°. From the principle of series and parallel mode, it follows that pump 1 and pump 2 operate in exactly opposite modes. Pump 1 draws oil while pump 2 discharges oil and pump 1 discharges oil while pump 2 draws oil. Therefore, the phase difference between the drive signals of pump 1 and pump 2 is set to 180°. When the solenoid-operated proportional valve spool is in position 1, as shown in figure 4(a), the DMEHA moves upward. In the first half cycle, pump 1 draws oil from the upper side of the hydraulic cylinder, and pump 2 discharges oil to the lower side of the hydraulic cylinder, performing one upward movement of the DMEHA. In the second half cycle, pump 1 discharges oil to the lower side, and pump 2 draws oil from the upper side of the hydraulic cylinder to perform an upward movement of the DMEHA. When the spool is in position 2, as shown in figure 4(b), the two piezoelectric stack pumps discharge high-pressure oil to the upper side of the hydraulic cylinder and low-pressure oil to the lower side of the hydraulic cylinder to realize the downward movement of the DMEHA.

3. Dynamic model of the DMEHA

Based on the structure of DMEHA, the mathematical model is divided into five major parts, i.e. the piezo-stack pump (PSP) model, the pump chamber model, the valve model, the fluid motion model, and the hydraulic cylinder model.

3.1. The PSP model

As the driver of the DMEHA, the PSP performs as a movable piezoelectric piston to the linear oscillation pump. The PSP is mainly composed of an axial dual-mounted piezoelectric stack actuator (ADPSA) and a linear piston.

3.2. The ADPSA structure

In order to realize large displacement, acceptable output force, and high-frequency response simultaneously, the ADPSA was designed as shown in figure 5. When excited by input voltage, the output displacement generated by the square piezoelectric stacks is transmitted to the output rod. Disc springs are employed to generate pre-compression due to the piezoelectric material cannot withstand tension.

3.3. The dynamic hysteresis force model

The frequency-dependent hysteresis with respect to inherent properties of piezoelectric material is harmful to the high-precision displacement control of the ADPSA. Therefore, it is essential to establish an accurate hysteresis model of the ADPSA.

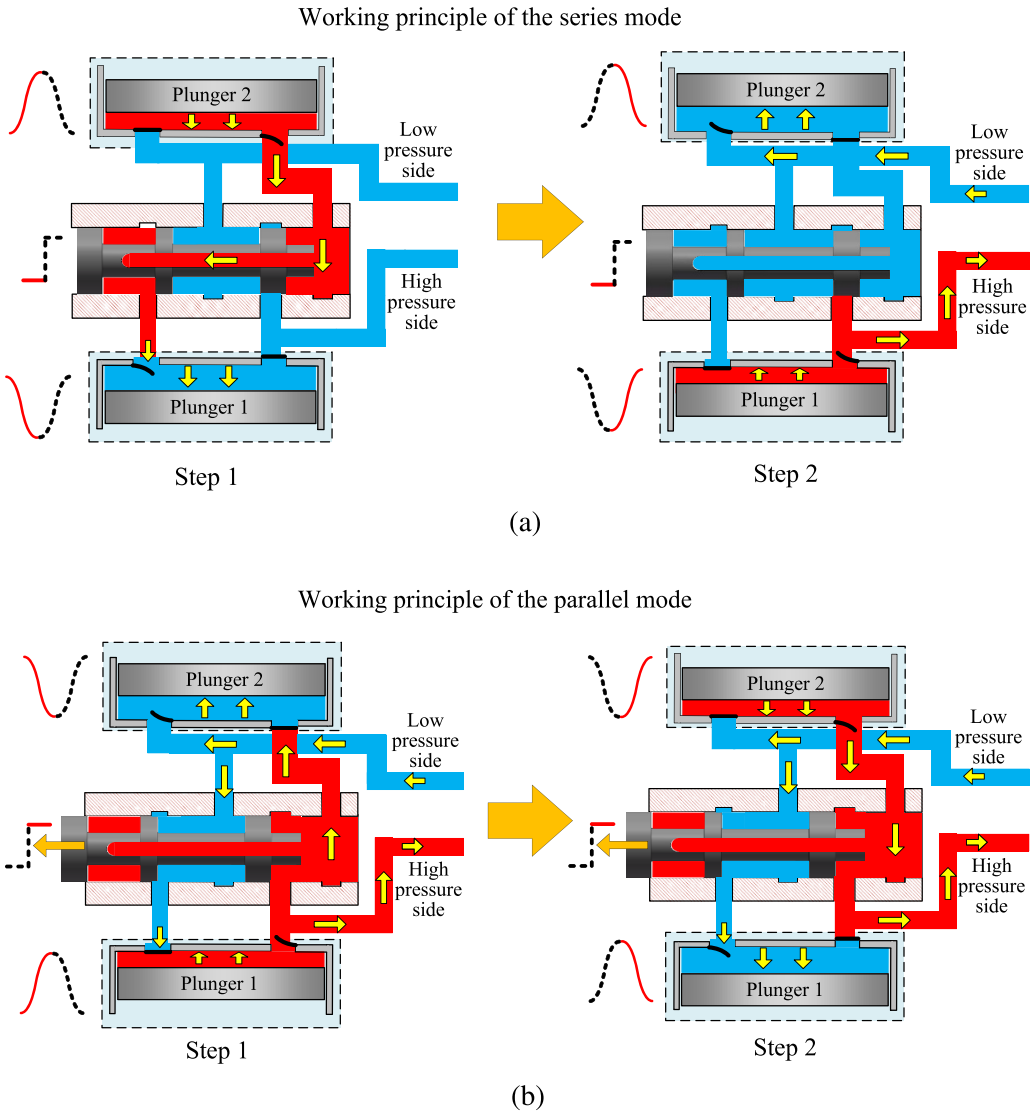

Figure 3. The switch of working mode. (a) The series mode. (b) The parallel mode.

First, a static hysteresis force model based on the asymmetric P-I model was established.

$$y = \begin{cases} w(u-r) & u - y/w = r \\ c & -r < u - y/w < r \\ w(u+r) & u - y/w = -r \end{cases} \tag{5}$$

$$y(t) = w \cdot \max u(t) - r, \min[u(t) + r, y(t-T)] \tag{6}$$

where u is the input, y is the output, r is the threshold value, w is the weight value, t is the time and T is the sampling period.

A single Backlash operator cannot fully describe the hysteresis of a piezoelectric stack. Therefore, a PI hysteresis model of a piezoelectric stack is generated by weighted stacking of n Backlash operators with different thresholds:

$$y(t) = w^T H_r[u, y_0](t) \tag{7}$$

$$H_r[u, y_0](t) = \max u(t) - r_i, \min[u(t) + r_i, y_i(t-T)] \tag{8}$$

where $W^T = [w_1, w_2 \ldots w_n]$ is the weight coefficient vector, $0 < r_1 < r_2 < \ldots < r_n$ is the threshold value, and y_0 is the initial output value.

The traditional PI model can characterize the hysteresis of the piezoelectric stack to some extent, but it cannot accurately describe the severe nonlinearity of the hysteresis of the piezoelectric stack. Therefore, according to the characteristics of the hysteresis curve of the piezoelectric stack, the input primary term and quadratic term are introduced, and the dead zone operator is used in series with the traditional PI model to improve the accuracy of the model. The rate correlation of output hysteresis of the piezoelectric stack is described by introducing a first-order inertia link. Finally, the expression of the improved PI hysteresis model is:

$$y(t) = \frac{k}{\tau} e^{-t/\tau} u + a u(t) + b u^2(t) + P^T S_q W^T H_r[u, y_0](t) \tag{9}$$

$$S_q[u](t) = \begin{cases} \max[u(t) - q_i, 0] & q_i > 0 \\ u(t) & q_i = 0 \end{cases} \tag{10}$$

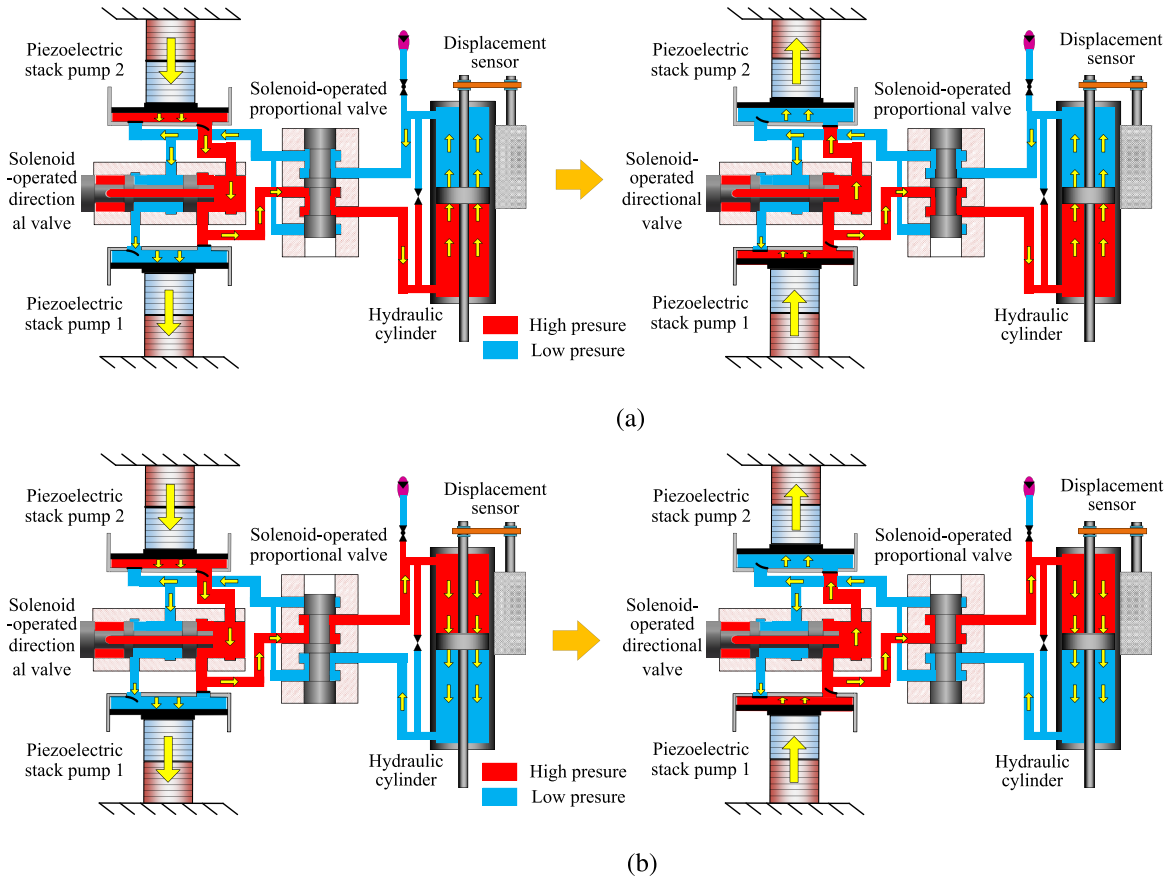

Figure 4. The working principle of the DMEHA. (a) The upward movement of the DMEHA. (b) The downward movement of the DMEHA.

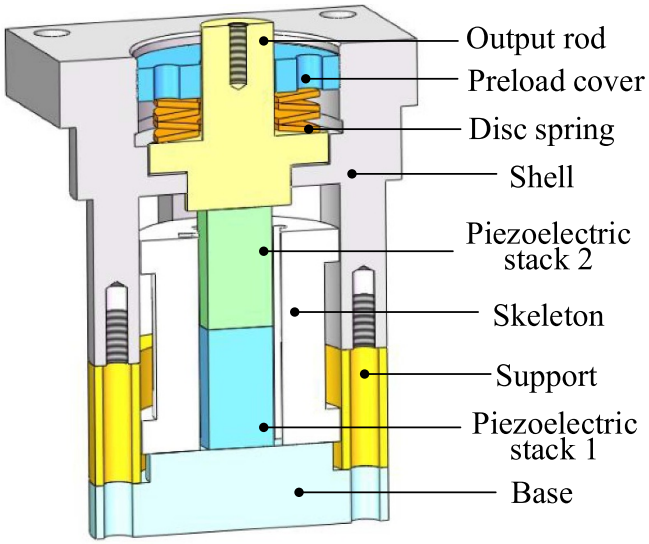

Figure 5. Structure of the ADPSA.

where $P^T = [p_1, p_2, \ldots, p_m]$ is the weight coefficient vector of the dead-zone operator, $0 = q_1 < q_2 < \ldots < q_m$ is the threshold, a and b are the coefficients, τ is the time constant and K is the coefficient.

The rate-dependent hysteresis force model is as follows:

$$f_i = k_i y(t) \tag{11}$$

where k_i is the stiffness of piezoelectric stack.

3.3.1. The ADPSA Multi-body dynamic model. The output rod, disc spring, and other components will also affect the output displacement of ADPSA as shown in figure 6. Therefore, a hysteresis considering a multi-body dynamic model is established as follows:

$$\begin{cases} m_{1e}\ddot{x}_1 = f_1 - k_1 u_1 - c_1\dot{x}_1 - k_2(x_1 - x_2) - c_2(\dot{x}_1 - \dot{x}_2) - f_2 \\ m_{2e}\ddot{x}_2 = f_2 + k_2(x_1 - x_2) + c_2(\dot{x}_1 - \dot{x}_2) - k_3(x_2 - x_3) - c_3(\dot{x}_2 - \dot{x}_3) \\ m_3\ddot{x}_3 = k_3(x_2 - x_3) + c_3(\dot{x}_2 - \dot{x}_3) - k_4 x_3 - c_4\dot{x}_3 \end{cases} \tag{12}$$

where m_{1e}, k_1, c_1, f_1, x_1 and m_{2e}, k_2, c_2, f_2, x_2 is the mass, stiffness, damping constant, output force, output displacement of square piezoelectric stack 1 and square piezoelectric stack 2 respectively, m_3, k_3, c_3 is the mass, stiffness and damping constant of output rod, k_4, c_4 is the stiffness and damping constant of disc spring.

3.3.2. The PSP dynamic model. Based on the ADPSA dynamic model, the PSP dynamic model is established by adding the piston to the ADPSA

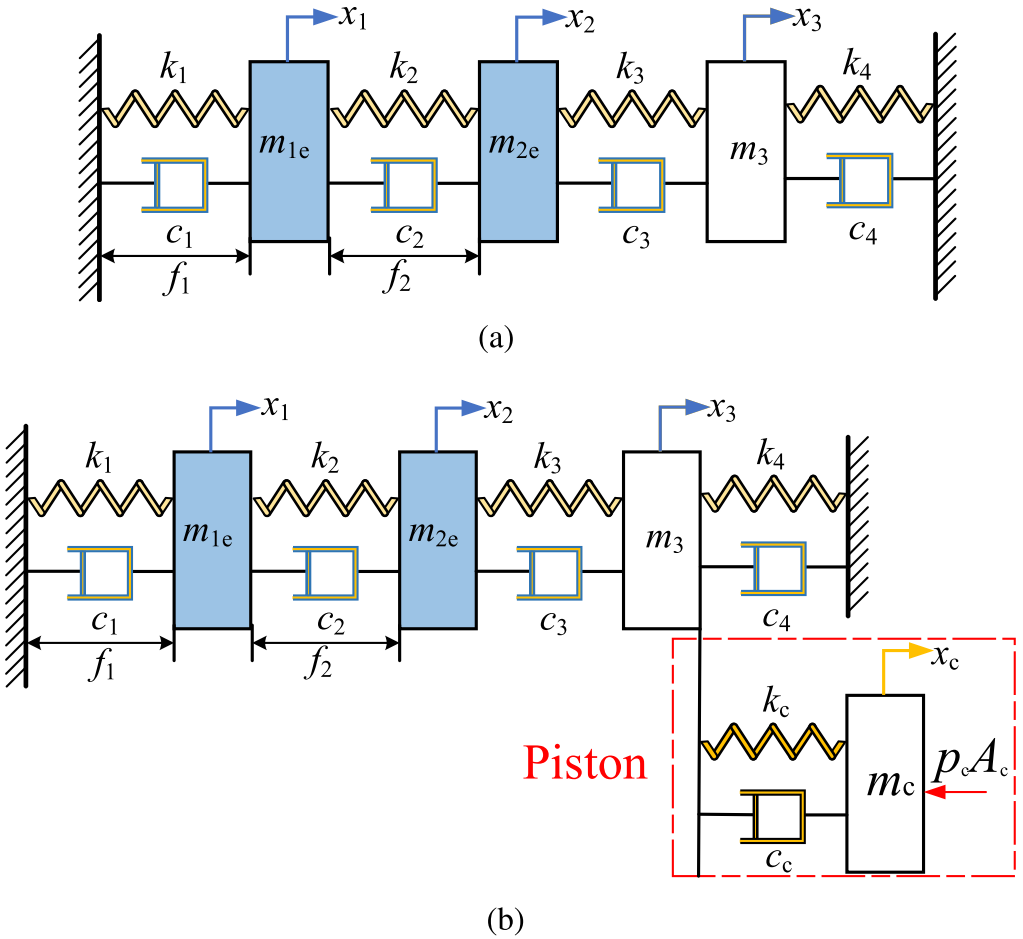

Figure 6. The multi-body dynamic model. (a) The dynamic model of ADPSA. (b) The dynamic model of PSP.

$$\begin{cases} m_{1e}\ddot{x}_1 = f_1 - k_1u_1 - c_1\dot{x}_1 - k_2(x_1 - x_2) - c_2(\dot{x}_1 - \dot{x}_2) - f_2 \\ m_{2e}\ddot{x}_2 = f_2 + k_2(x_1 - x_2) + c_2(\dot{x}_1 - \dot{x}_2) - k_3(x_2 - x_3) - c_3(\dot{x}_2 - \dot{x}_3) \\ m_3\ddot{x}_3 = k_3(x_2 - x_3) + c_3(\dot{x}_2 - \dot{x}_3) - k_4x_3 - c_4\dot{x}_3 - k_c(x_3 - x_c) - c_c(\dot{x}_3 - \dot{x}_c) \\ m_c\ddot{x}_c = k_c(x_3 - x_c) + c_c(\dot{x}_3 - \dot{x}_c) - p_cA_c \end{cases} \tag{13}$$

where k_c and c_c are the stiffness and damping constant of piston, p_c is pressure of pump chamber and A_c is cross-sectional area of piston.

3.4. The pump chamber model

The variation of pressure in pump chambers is subjected to the compressibility of hydraulic oil and represented by the effective bulk modulus. The effective bulk modulus of hydraulic oil β_c is defined by using the volume and its derivative. This correlation is given as:

$$\beta_c = -V_c\frac{\dot{P}_c}{\dot{V}_c} \tag{14}$$

where V_c represents the volume of fluid.

In reality, the effective bulk modulus of hydraulic oil is dependent on the content of entrapped air, and is represented by the equation:

$$\frac{1}{\beta_{ce}} = \lambda_a\frac{p_a}{p_o^2} + \left(1 - \lambda_a\frac{p_a}{p_o}\right)\frac{1}{\beta_o} \tag{15}$$

where p_a is atmospheric pressure, λ_a is fraction of entrapped air, p_o is applying pressure on the oil, and β_o is bulk modulus of pure oil.

The pressure p_c of the oil in the pump chamber can be described as:

$$\dot{p}_c = \beta_{ce}\frac{Q_{in} - Q_{out} + A_c\dot{u}_c}{A_c(h - u_c)} \tag{16}$$

where Q_{in} and Q_{out} represent the inlet and outlet oil respectively, A_c is the cross-sectional area of the piston in the pump

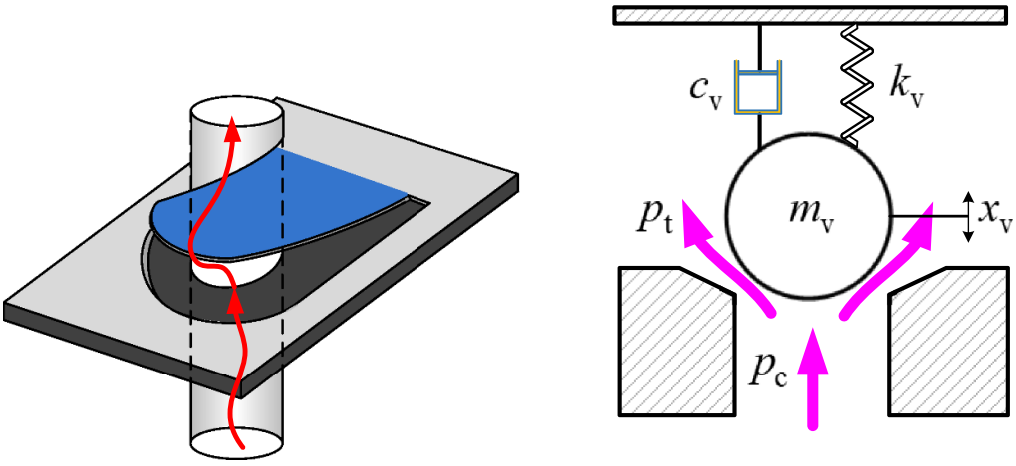

(a) Schematic diagram of cantilever reed valve (b) Equivalent dynamics model

Figure 7. The dynamic model for cantilever reed valve.

chamber, h is the height of the pump chamber, and u_c is the displacement of the piston.

3.5. The valve model

The cantilever reed valve in the pump chamber is actually a one-way valve. Its function is to realize the independence of oil absorption and discharge in a single pump cavity. When the pressure difference between the pump chamber and the pipeline accumulates and arrives at a certain threshold, the deformed cantilever reed valve performs as a passive check valve, as shown in figure 7.

The open/close of the cantilever reed valve subjected to the pressure differential is regarded as a complex fluid-solid interaction process and fails to be modeled by the accurate mathematical model. The equivalent single-degree-of-freedom system is applied to address this issue.

According to the vibration equation, the dynamic process of the cantilever suctioned and discharged reed valve is described as follows:

$$m_v\ddot{x}_{vo} + c_v\dot{x}_{vo} + k_v x_{vo} = A_v\Delta p = A_v(p_c - p_{th}) \tag{17}$$

$$m_v\ddot{x}_{vi} + c_v\dot{x}_{vi} + k_v x_{vi} = A_v\Delta p = A_v(p_{tl} - p_c) \tag{18}$$

where m_v, c_v and k_v are the equivalent mass, equivalent damping coefficient, and equivalent stiffness of the cantilever reed valve; x_{vo} and x_{vi} are the equivalent opening of the two cantilever reed valves respectively; A_v is the equivalent opening area of the cantilever reed valve; p_{th} and p_{tl} are the pressure of the high and low-pressure pipelines respectively; p_c is the pressure value in the pump chamber.

The flowrate across the cantilever reed valve is modeled by using the turbulent orifice flow, and represented as:

$$Q_{in} = sgn(p_{tl} - p_c)C_{dv}w_v x_{vi}\sqrt{\frac{2}{\rho}|p_{tl} - p_c|} \tag{19}$$

$$Q_{out} = sgn(p_c - p_{th})C_{dv}w_v x_{vo}\sqrt{\frac{2}{\rho}|p_c - p_{th}|} \tag{20}$$

where C_{dv} is the flow coefficient of the cantilever reed valve port; w_v is the orifice area gradient.

The equations for the output pressure and flow rate of the EHA in series and parallel mode are mentioned in section 2, respectively. However, this is under ideal conditions. In practice, there is local loss at the solenoid valve, which can be reduced to liquid resistance.

In series mode, during the first half of a cycle, the oil is discharged by pump 2 and passes through the solenoid-operated directional control valve into pump 1. p_{h2} is the pressure of the high-pressure tube corresponding to pump 2, p_{l1} is the pressure of the low-pressure tube corresponding to pump 1, Q_{in1} and Q_{out2} are the flow rate of pump 1 suction fluid and pump 2 discharge fluid respectively. Then the relationship between them can be expressed by the following equation:

$$p_{h2} - p_{l1} = Q_{in1}R_{sd} \tag{21}$$

$$\dot{p}_{h2} = \beta_{ce}\frac{Q_{out2} - Q_{in1}}{V_{ed}} \tag{22}$$

where R_{sd} is the equivalent liquid resistance of the solenoid-operated directional control valve and V_{ed} denotes the volume in the solenoid-operated directional control valve cavity.

In parallel mode, pump 1 and pump 2 alternately discharge and absorb oil. In one cycle, two suctions and two discharges are completed. Therefore, the relationship can be expressed as:

$$p_{h2} - p_{vh1} = Q_{out2}R_{sd} \tag{23}$$

$$p_{vl1} - p_{l1} = Q_{in1}R_{sd} \tag{24}$$

where p_{vh1} indicates the pressure on the side of the high-pressure tube connected to the solenoid-operated directional control valve, and p_{vl1} indicates the pressure on the side of the low-pressure tube connected to the solenoid-operated directional control valve.

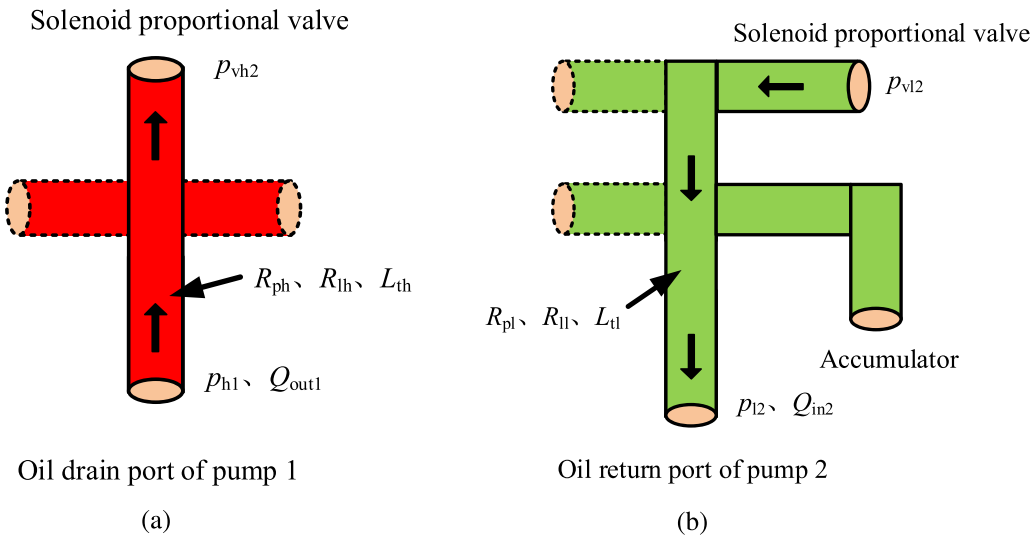

Figure 8. Equivalent piping in series mode. (a) High pressure tube. (b) Low pressure tube.

3.6. The fluid motion model

Similar to the electrical energy loss caused by resistance, inductance, and capacitance in the circuit, there are losses in the flow transmission within the tube, which are mainly caused by fluid resistance, liquid inductance, and liquid capacity. Linear fluid resistance R_t can be obtained as follow

$$R_t = \frac{\Delta p_{ll}}{Q} = \frac{128\mu_f l_t}{\pi D_t^4} \tag{25}$$

where μ_f is the fluid kinematic viscosity, l_t, D_t represent the length and diameter of the tube.

Besides the fluid resistance R_t, there also exists local fluid resistance R_j which can be described as follow

$$R_j = \frac{\Delta p_{pl}}{Q} = \xi \frac{8\rho Q}{\pi^2 D_t^4} \tag{26}$$

where Q represents the flow rate across the tube, and ξ is the local loss coefficient which is related to the structure of the tube.

Compared with the inductance in the circuit, there is also a liquid inductance in the fluid due to the fluid inertia within the tube, which can store the kinetic energy of the fluid. The size of the fluid inductance is related to the structure of the pipeline (tube diameter D_t and tube length l_t), which can be expressed as follows

$$L_t = \frac{4\rho l_t}{\pi D_t^2}. \tag{27}$$

3.6.1. The fluid motion model in series mode. In series mode, the tubes of two piezoelectric pumps are independent of each other. After simplification, the tubes can be divided into high-pressure and low-pressure tubes, as shown in figures 8(a) and (b). Then the models can be expressed as:

$$\text{high}-\text{pressure}: p_{h1} - p_{vh2} = (R_{lh} + R_{ph})Q_{out1} + L_{th}\dot{Q}_{out1} \tag{28}$$

$$\text{low}-\text{pressure}: p_{vl2} - p_{l2} = (R_{l1} + R_{p1})Q_{in2} + L_{tl}\dot{Q}_{in2} \tag{29}$$

where R_{lh}, R_{ph}, R_{ll}, R_{pl} are the along-range and local resistance of the high and low-pressure side tubes respectively.

For modeling purposes, the length of the tubes between the solenoid-operated proportional valve and the hydraulic cylinder is ignored. In series mode, the pressure-flow equation between the valve and the hydraulic cylinder is:

$$\text{high}-\text{pressure}\begin{cases} p_{vh2} - p_{ch} = Q_{out1}R_{sp} \\ \dot{p}_{vh2} = \beta_{ce}\frac{Q_{out1} - Q_{inc}}{V_{ep}} \end{cases} \tag{30}$$

$$\text{low}-\text{pressure}\begin{cases} p_{cl} - p_{vl2} = Q_{outc}R_{sp} \\ \dot{p}_{cl} = \beta_{ce}\frac{Q_{outc} - Q_{in2}}{V_{ep}} \end{cases}. \tag{31}$$

3.6.2. The fluid motion model in parallel mode. In parallel mode, the high-pressure tube and low-pressure tube fluid motion model is shown in figures 9(a) and (b) respectively.

Then the high-pressure tube and low-pressure tube are modeled respectively as follows

$$\text{high}-\text{pressure}\begin{cases} p_{h1} - p_{vh2} = (R_{lh1} + R_{ph1})Q_{out1} + L_{th1}\dot{Q}_{out1} \\ p_{vh1} - p_{vh2} = (R_{lh2} + R_{ph2})Q_{out2} + L_{th2}\dot{Q}_{out2} \end{cases} \tag{32}$$

$$\text{low}-\text{pressure}\begin{cases} p_{vl2} - p_{vl1} = (R_{ll1} + R_{pl1})Q_{in1} + L_{tl1}\dot{Q}_{in1} \\ p_{vl2} - p_{l2} = (R_{ll2} + R_{pl2})Q_{in2} + L_{tl2}\dot{Q}_{in2} \end{cases} \tag{33}$$

where p_{h1}, p_{vh2} are the pressure of the high-pressure tube connected to pump 1 and the solenoid-operated proportional valve respectively, p_{l2}, p_{vl2} are the pressure of the low-pressure tube connected to pump 2 and the solenoid-operated proportional valve respectively. Q_{in2} and Q_{out1} are the flow rates of pump two suction oil and pump 1 discharge oil, respectively. R_{lh1}, R_{ph1} and R_{lh2}, R_{ph2} are the along-range and local liquid resistance of the high-pressure side pipeline of pump 1 and pump 2 respectively, and R_{ll1}, R_{pl1} and R_{ll2}, R_{pl2} are the along-range

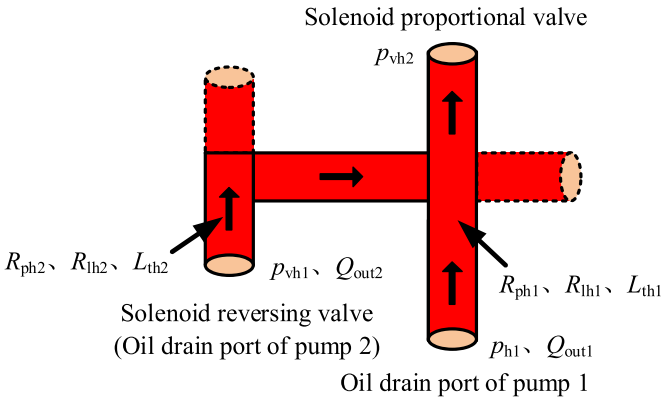

(a) High pressure tube

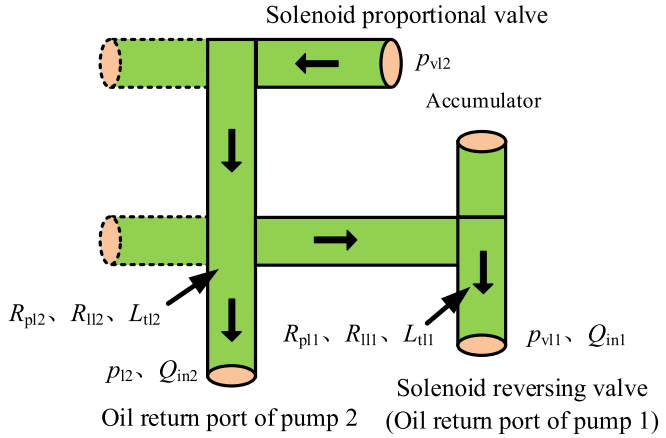

(b) Low pressure tube

Figure 9. Equivalent piping in parallel mode.

and local liquid resistance of the low-pressure side pipeline of pump 1 and pump 2 respectively. L_{th} and L_{tl} indicate the liquid sense on the high and low-pressure side, respectively.

The high-pressure and low-pressure tubes are connected to the hydraulic cylinder by a solenoid-operated proportional valve. Due to the short length of the connection line between the valve and the hydraulic cylinder, the line pressure is approximated to be equal for modeling purposes. In parallel mode, the pressure-flow equation between the valve and the hydraulic cylinder is as follows:

$$\text{high}-\text{pressure}\begin{cases} p_{vh2}-p_{ch}=Q_{out0}R_{sp} \\ \dot{p}_{vh2}=\beta_{ce}\frac{Q_{out0}-Q_{inc}}{V_{ep}} \end{cases} \tag{34}$$

$$\text{low}-\text{pressure}\begin{cases} p_{cl}-p_{vl2}=Q_{in0}R_{sp} \\ \dot{p}_{cl}=\beta_{ce}\frac{Q_{outc}-Q_{in0}}{V_{ep}} \end{cases} \tag{35}$$

where R_{sp}, V_{ep} is the equivalent liquid resistance and cavity volume of the solenoid-operated proportional valve, Q_{inc}, Q_{outc} are the flow rate into and out of the hydraulic cylinder, p_{ch}, p_{cl} are the high-pressure and low-pressure chamber fluid pressure, respectively, $Q_{in0}=Q_{in1}+Q_{in2}$, $Q_{out0}=Q_{out1}+Q_{out2}$.

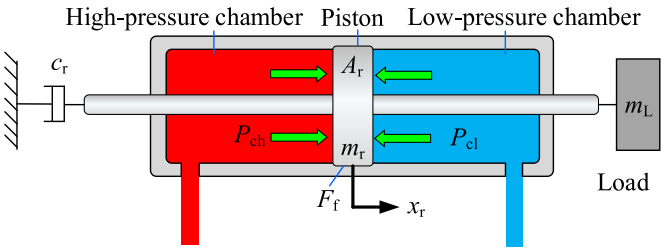

Figure 10. Hydraulic cylinder.

3.7. The hydraulic cylinder model

As it is shown in figure 10, the output rod of the hydraulic cylinder exhibits motion due to the pressure difference between two sides. However, the output rod is also subjected to friction, viscous and gravity during process of motion. According to Newton's laws of motion and kinetic equations in general, the hydraulic cylinder model can be described as follows:

$$(m_r+m_L)\ddot{x}_r+c_r\dot{x}_r=(p_{ch}-p_{cl})A_r-(m_r+m_L)g-F_f \tag{36}$$

where m_r and m_L represent the mass of output rod and load. c_r is the damping constant of output rod. p_{ch} and p_{cl} are the high pressure and low pressure of two sides in hydraulic cylinder. F_f is the friction force between the hydraulic cylinder piston and the hydraulic cylinder wall during the motion. The frictional force F_f is related to the speed of the piston, so it is necessary to select a suitable model for modeling the frictional force. The LuGre model was selected [36], which is expressed as follows:

$$F_f(v_c)=\left[F_c+(F_s-F_c)e^{-\left|\frac{v_c}{v_s}\right|}\right]sgn(v_c)+Bv_c \tag{37}$$

$$\text{sgn}(v_c)=\begin{cases} \frac{v_c}{|v_c|}, |v_c|>\Delta v \\ 0, \text{else} \end{cases} \tag{38}$$

where v_c is the velocity of hydraulic cylinder piston, v_s is the Stribeck velocity, F_c denotes the coulomb friction force on the piston, F_s denotes the static friction force on the piston, Δ_v is the dynamic and static friction threshold, and B denotes the coefficient of viscous friction.

There are unknown parameters F_c, F_s, v_s, and B in the friction force model, which is difficult to be measured directly by experiments, so parameter identification is needed. Based on the parameter estimation toolbox in MATLAB/Simulink, the parameters are identified. The identification results are $F_c=-29.9\,\text{N}$, $F_s=48.5\,\text{N}$, $v_s=0.034\,\text{m s}^{-1}$, $B=808.9\,\text{Ns m}^{-1}$. The identified parameters were added to the friction model.

4. Parameters estimation and experimental verification

Based on the dynamic hysteresis model, the dynamic model of the ADPSA can be implemented. However, there are still several parameters that need to be identified. To simplify the identification process, the model is divided into a quasi-static part and a frequency-dependent part as figure 11 shows, and

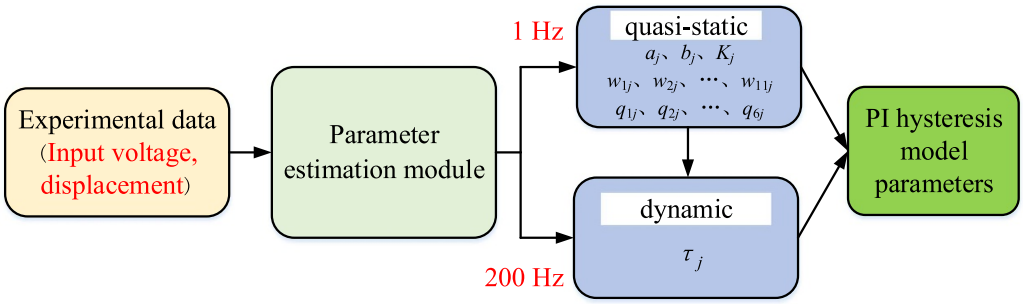

Figure 11. The parameter identification methodology.

Table 2. Result of parameter estimation.

Symbol	Value	Symbol	Value	Symbol	Value
w_{11}	−0.014	w_{12}	−0.109	w_{21}	0.057
w_{22}	0.080	w_{31}	−0.040	w_{32}	0.041
w_{41}	0	w_{42}	0	w_{51}	0.053
w_{52}	0.066	w_{61}	−0.099	w_{62}	−0.229
w_{71}	0.117	w_{72}	0.178	w_{81}	−0.027
w_{82}	0.012	w_{91}	0	w_{92}	0
w_{101}	0.014	w_{102}	0.031	w_{111}	−0.019
w_{112}	0.099	p_{11}	0.721	p_{12}	−0.477
p_{21}	1.576	p_{22}	1.137	p_{31}	0.500
p_{32}	0.571	p_{41}	−0.067	p_{42}	−0.071
p_{51}	−0.684	p_{52}	−0.616	p_{61}	0.113
p_{62}	0.571	a_1	−0.029	b_1	-6.9×10^{-5}
k_1	0.150	τ_1	5.32×10^{-5}	a_2	−0.026
b_2	1.33×10^{-4}	k_2	0.227	τ_2	2.84×10^{-5}

a parameter identification methodology based on the least square method is utilized. The criterion of parameter convergence is to minimize the sum of squares of error and the objective function is expressed as follows

$$e(a,b,l,\tau,w_1,w_2,\ldots,w_{11},p_1,p_2,\ldots,p_6) = \min \sum_{j=1}^{z} (y_{\mathrm{aj}} - y_{\mathrm{sj}}^{s})^2. \tag{39}$$

where y_{a} and y_{s} represent the actual and simulated output displacements respectively; z denote the total samples.

There are some normal methods of parameter estimation such as neural network optimization algorithm, particle swarm optimization algorithm, topology optimization algorithm and so on which are difficult to utilization. Thus, a method of parameter estimation integration in MATLAB/Simulink which exhibits conventional, rapid, and accurate is employed in this article.

4.1. Parameters estimation

Utilizing the experimental output displacement of the piezoelectric stack under the driving signal of 140 V 1 Hz for parameter estimation of the quasi-static part. As for the parameter τ_{j} of the frequency-dependent part, the experimental output displacement of the piezoelectric stack under the driving signal of 140 V 200 Hz was employed with the parameters of the quasi-static part substituted into the model. The result of parameter estimation is shown in table 2, the other parameters in the dynamic model are shown in table 3, and the size of the piezoelectric stack is shown in table 4.

Table 3. The other parameters in the dynamic hysteresis model.

Name	Symbol	Value	Unit
Lower piezoelectric stack mass	m_1	0.014	kg
Upper piezoelectric stack mass	m_2	0.018	kg
Output rod mass	m_3	0.038	kg
Lower piezoelectric stack stiffness	k_1	180	$\mathrm{N}\mu\mathrm{m}^{-1}$
Upper piezoelectric stack stiffness	k_2	250	$\mathrm{N}\mu\mathrm{m}^{-1}$
Output rod stiffness	k_3	4347	$\mathrm{N}\mu\mathrm{m}^{-1}$
Belleville spring stiffness	k_4	0.212	$\mathrm{N}\mu\mathrm{m}^{-1}$
Lower piezoelectric stack damp	c_1	1200	Nsm^{-1}
Upper piezoelectric stack damp	c_2	1400	Nsm^{-1}
Output rod damp	c_3	850	Nsm^{-1}
Belleville spring damp	c_4	660	Nsm^{-1}

4.2. Experimental verification

The ADPSA was presented experimentally as figure 12 and shows to verify the effectiveness of the established hysteresis model and parameters estimation method.

The experimental system consists of a signal general (Beijing Puyuan Jingdian Technology Co., LTD, DG1022), eddy current displacement sensor (Hangzhou

Table 4. The dimension parameters of the piezoelectric pump.

Name	Value	Unit
Length of the piezoelectric stack	18	mm
Sectional of the piezoelectric stack	10×10	mm
Height of the ADPSA	72	mm
Diameter of the ADPSA	45	mm
Diameter of the piston	46	mm
Diameter of the cantilever reed valve	6	mm
Thickness of the cantilever reed valve	0.15	mm

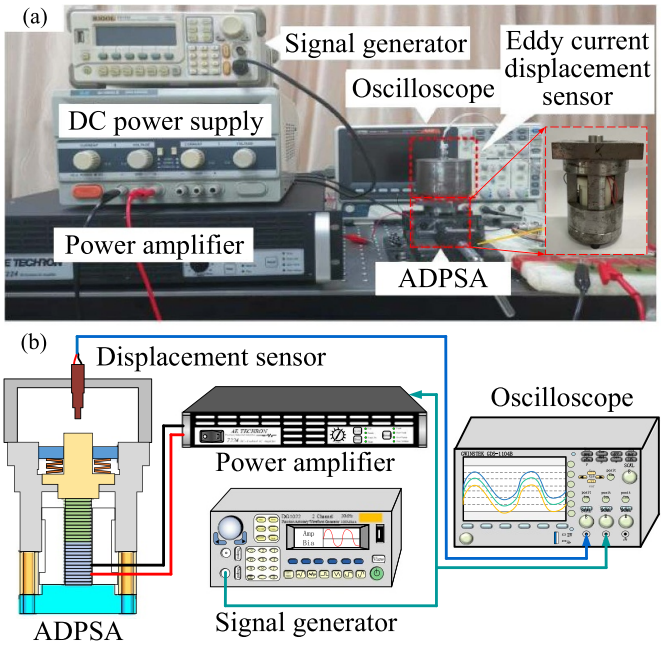

Figure 12. The test bench of the ADPSA.

Huarui Instrument Co., LTD, CZF-2), power amplifier (AE Techron Inc. 7224), VDC power, oscilloscope (Taiwan Cuswell Electronics, GDS-1104B) and the ADPSA. The driving signal generated by signal general is amplified by a power amplifier to drive the piezoelectric stack (Harbin soluble core technology CO., LTD, pst-150-10×10-20). The output displacement of the ADPSA collected by the eddy-current displacement sensor is displayed on an oscilloscope.

The experiments of two piezoelectric stacks were carried out respectively under the driving signal of 140 V within the frequency range of 1–200 Hz and the results are shown as figure 13. It can be seen from the comparison between the experiment and simulation that the dynamic hysteresis model has an excellent ability to describe the output characteristic.

5. Experimental evaluations

5.1. Prototype and test bench of the DPEHA

The experimental test bench of DMEHA is shown in figure 14. It mainly includes DMEHA, signal generator (AFG-225, Gwinstek), laser displacement sensor (CD33-120 N-422, Sixin), and power amplifier (7224, AETechron). The signals to drive the two piezoelectric stack pumps are generated by the signal generator and amplified by the power amplifier. The laser displacement sensor measures the displacement of the hydraulic cylinder. The measured data is transferred to the host computer and calculated for the output flow of the DMEHA. In addition, a spring-loaded accumulator is required to provide a bias pressure to the system during the experiment. The bias pressure provided by the accumulator in this experiment is 0.8 MPa.

5.2. Performance verification of the DMEHA

The output performance of the DMEHA is tested in series and parallel mode respectively, and compared with the simulation results to verify the accuracy of the established simulation model. What's more, the effect of drive frequency, drive voltage, and load weight on the output performance of the DMEHA is investigated.

5.2.1. Series mode. The drive voltage amplitudes of the two pumps were set to 40 V, 60 V, 80 V, 100 V, and 120 V to test the output flow rate of the DMEHA at different frequencies. The experimental results are shown in figure 15. The maximum flow rate at each voltage amplitude is selected and compared with the simulation results to obtain figure 16. It can be seen from the experimental results that the maximum output flow rate of the DMEHA can reach 1.17 l min^{-1} at the driving voltage amplitude of 120 V and frequency of 360 Hz. As the drive voltage amplitude increases from 40 V to 120 V, the maximum output flow of the DMEHA increases approximately and linearly, and the changing pattern is consistent with the simulation results. It can also be observed that at the same drive voltage amplitude, the output flow of the DMEHA tends to increase and then decrease as the frequency of the drive voltage increases, and the peak output flow almost always occurs around 340 Hz.

The experimental results of the DMEHA are compared with the simulation results at the voltage amplitude of 100 V and 120 V, as shown in figures 17 and 18. The simulated values are larger than the experimental values at low frequencies. Still, the simulated and experimental curves almost match at high frequencies, indicating that the established simulation model is more accurate and can predict the output characteristics of the DMEHA.

The output flow rate of the DMEHA with load was tested. The load mass was increased from 2 kg to 20 kg, and the load-flow characteristics of the DMEHA were obtained, as shown in figure 19. In series mode, the output flow of the DMEHA decreases more slowly with increasing load mass. With a load mass of 20 kg, the DMEHA still outputs a flow rate of 0.56 l min^{-1}. Therefore, it is predicted that the DMEHA can carry a maximum load of about 40 kg in series mode.

5.2.2. Parallel mode. The curve of the output flow of DMEHA in parallel mode with frequency for different voltage amplitudes is shown in figure 20. A comparison of the experimental and simulation results for the maximum output

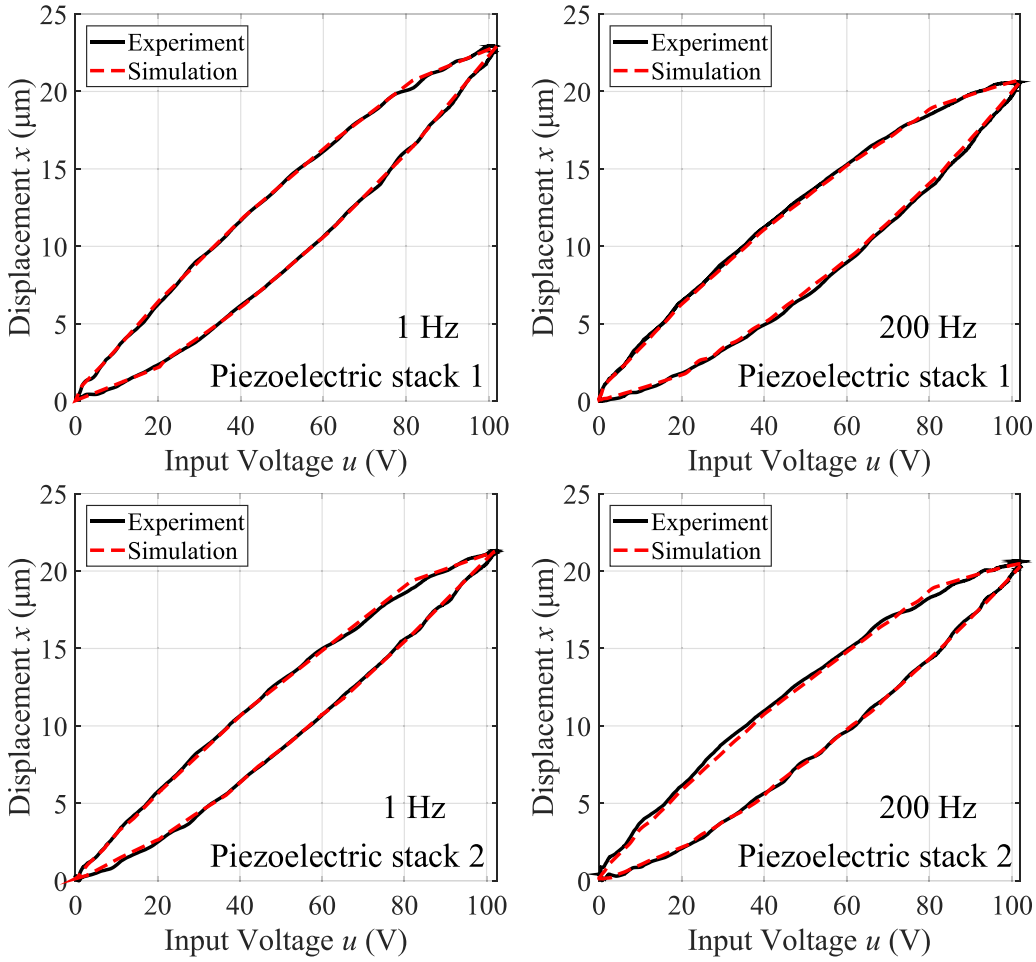

Figure 13. The experimental verification.

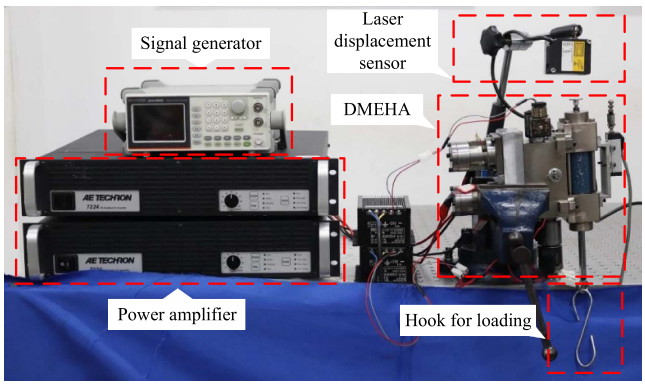

Figure 14. The experimental test bench of the DMEHA.

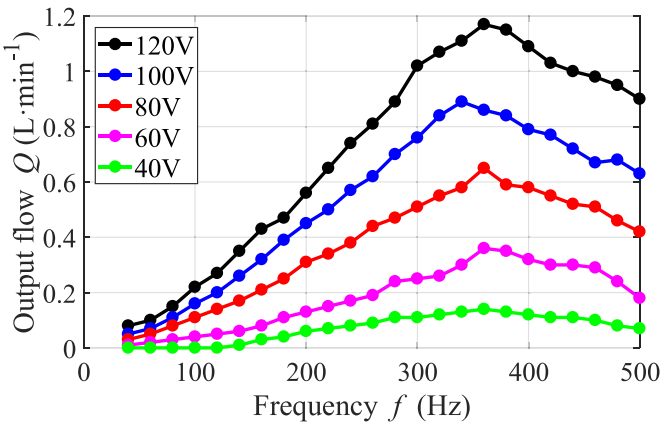

Figure 15. The output flow rate of the DMEHA in series mode.

flow rate at different amplitudes is shown in figure 21. The experimental results show that the maximum output flow rate of the DMEHA can reach 1.97 1min^{-1} under the driving voltage amplitude of 120 V and frequency of 420 Hz. As the driving voltage amplitude increases from 40 V to 120 V, the maximum output flow rate of the DMEHA increases approximately linearly, and the change law is consistent with the simulation results. The output flow rate also shows a trend of increasing and then decreasing with frequency and reaches the maximum output flow rate near 420 Hz.

Figures 22 and 23 show the comparison of experimental and simulation results for the DMEHA at the drive voltage amplitude of 100 V and 120 V, respectively. The comparison results show that the frequency-flow curves of the DMEHA in parallel mode have the same trend, which again proves the accuracy of the established simulation model.

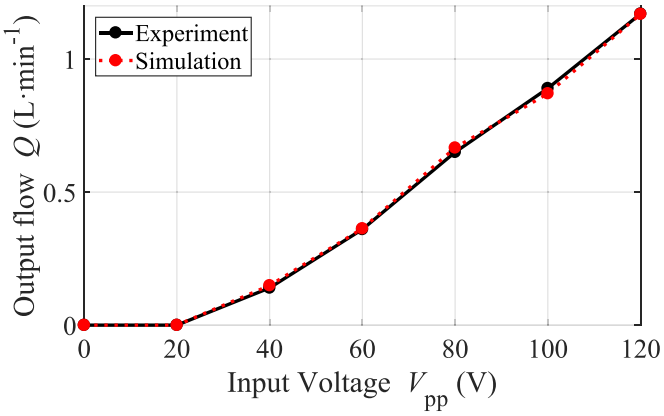

Figure 16. The maximum flow rate at each voltage amplitude in series mode.

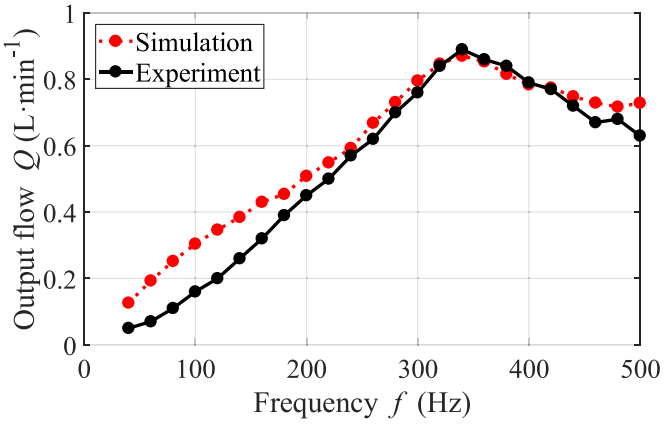

Figure 17. The verification of dynamic model at 100 V.

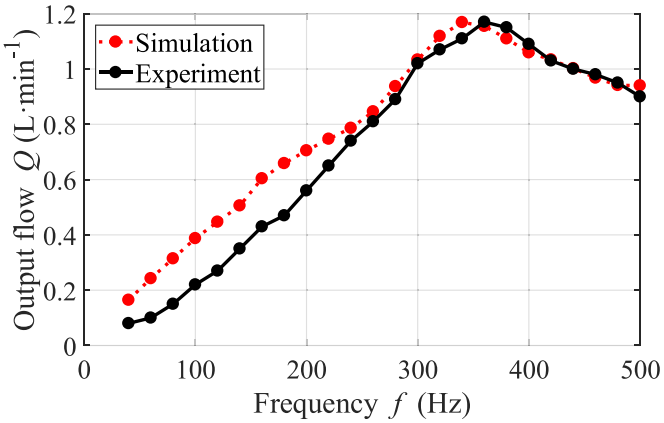

Figure 18. The verification of dynamic model at 120 V.

The output flow rate variation of the DMEHA with load in parallel mode was tested, as shown in figure 24. The output flow rate of the DMEHA in parallel mode decreases quickly with the increase of load mass. With a load of 20 kg, the DMEHA only has a flow output of 0.12 l min^{-1}. The output flow rate of the DMEHA only reaches 0.12 l min^{-1} with a load of 20 kg. The maximum load that the DMEHA can carry in parallel mode is predicted to be about 23 kg. Compared with

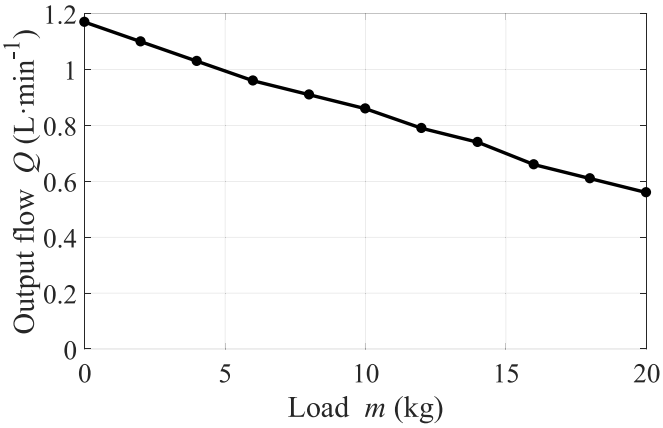

Figure 19. The load-flow characteristics of the DMEHA in series mode.

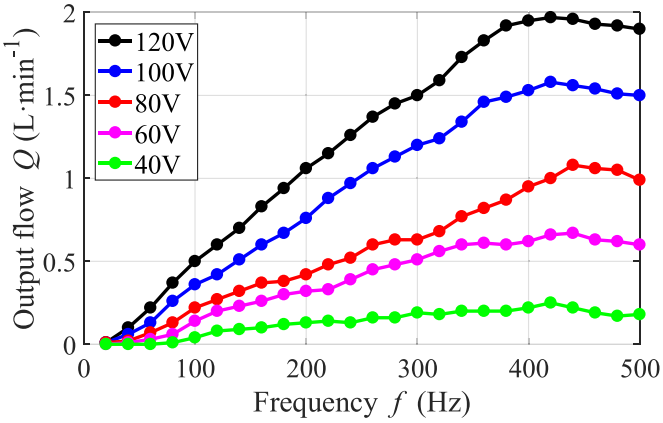

Figure 20. The output flow rate of the DMEHA at different frequencies in parallel mode.

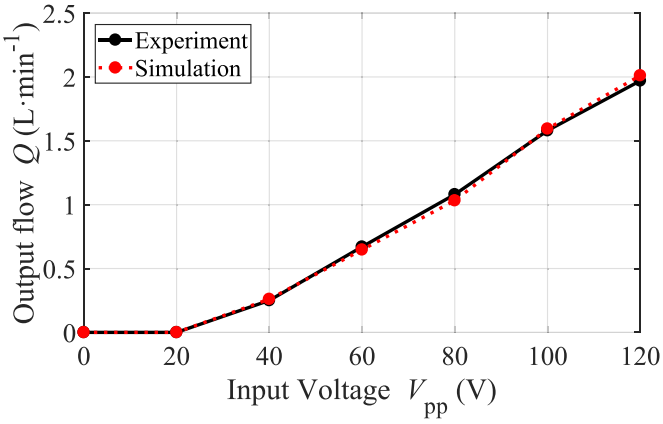

Figure 21. The maximum flow rate at each voltage amplitude in parallel mode.

the series mode, the output flow of the DMEHA is higher in the parallel mode, and the load-carrying capacity is weaker. It also confirms that the series mode is suitable for high-load applications, and the parallel mode is suitable for high-speed applications.

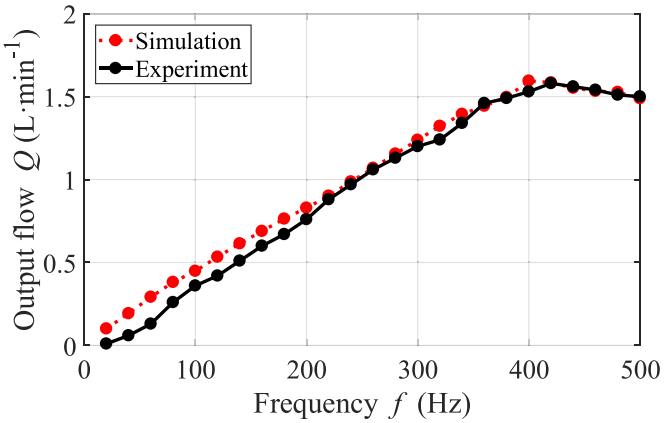

Figure 22. The verification of dynamic model at 100 V.

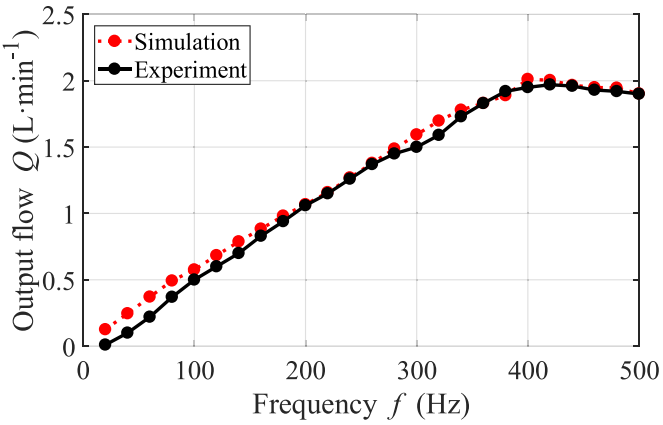

Figure 23. The verification of dynamic model at 120 V.

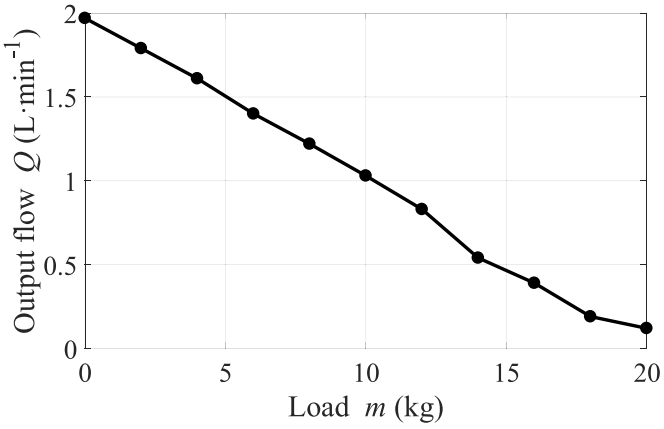

Figure 24. the load-flow characteristics of DMEHA in parallel mode.

The comparisons between the proposed DMEHA and some previous studies are listed in table 5. Compared with the piezoelectric hybrid actuator proposed in [37], the DMEHA has a larger unit flow and a same unit load capacity. compared with the piezo driven reed valve pump proposed in [38], the DMEHA has the advantages both in unit flow and unit load capacity.

Table 5. Comparison between the proposed DMEHA and other works.

Studies	Unit flow (ml min·V^{-1})	Unit pressure/load
Li *et al* [37]	1.13 (series)	4.6 N/V (series)
	1.5 (parallel)	2.35 N/V (parallel)
Woo *et al* [38]	12.6	40 Pa/V
This work	9.75 (series)	3.3 N/V (series)
	16.42 (parallel)	1.7 N/V (parallel)

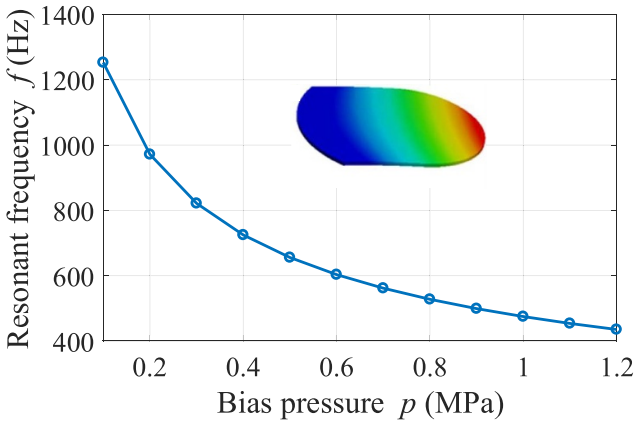

Figure 25. The resonant frequency of the cantilever valve at different pressure.

6. Discussion

6.1. The dynamic response

6.1.1. The resonant frequency of cantilever valve. The cantilever valve bends and deforms due to the differential pressure, creating a certain opening for the fluid to pass through. It is necessary to analyze the characteristics of the cantilever valve in the oil. Therefore, a wet modal analysis of the cantilever valve was carried out with the employment of ANSYS. The results are shown in figure 25, which indicated that the first-order resonant frequency of the cantilever valve decreases with the increase of fluid bias pressure. When the bias pressure is 0.8 MPa (The bias pressure of the DPEHA in this paper is 0.8 MPa), the first-order resonance frequency of this size cantilever valve piece is 527.6 Hz which can fulfill the needs of the operating frequency.

6.1.2. The step response of DMEHA. Based on the proposed analytical model, the step response of the DMEHA under different working mode is tested, the step amplitude is 8 mm. The step response of the DMEHA in series mode is shown in figure 26(a), the step response time is about 0.119 s and the overshoot is small, which indicates that the actuator has a good

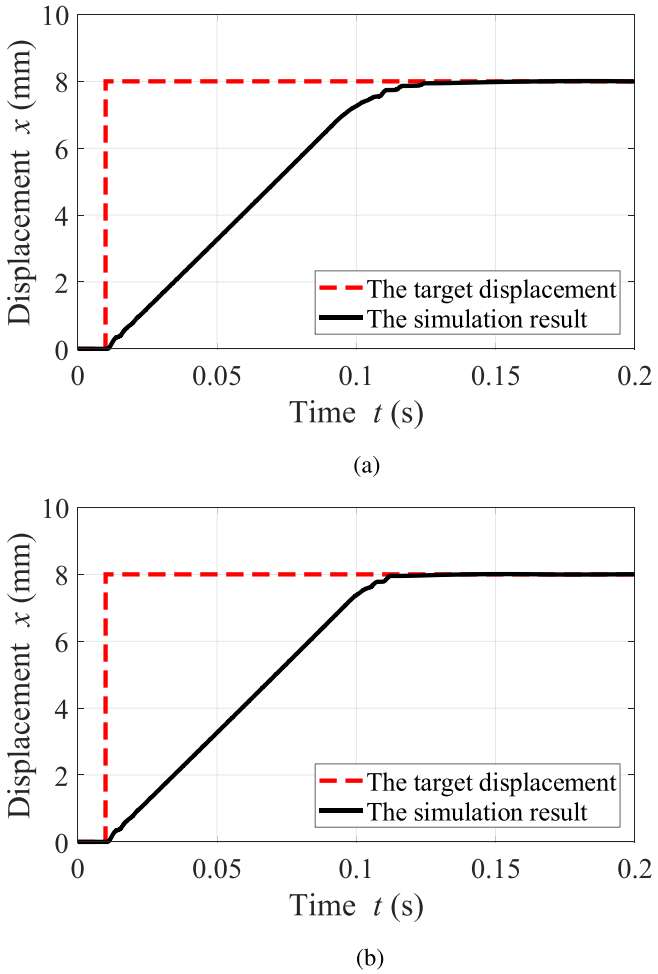

Figure 26. The step response of the DMEHA. (a) The step response in series mode. (b) The step response in parallel mode.

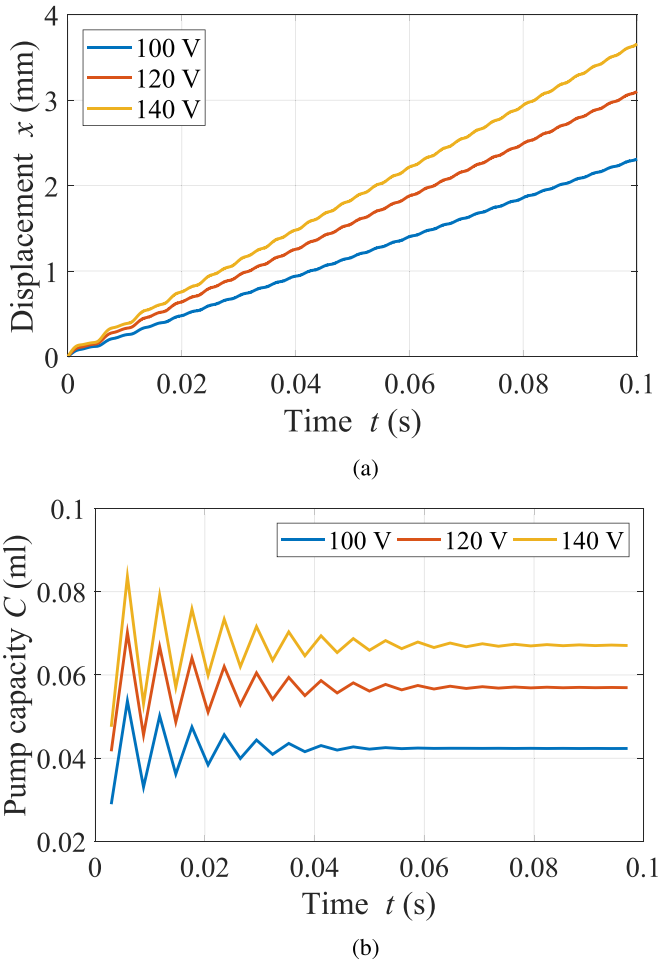

Figure 27. The repeatability of the piezoelectric pump. (a) The output displacement of the DPEHA. (b) The pump capacity in each plunger stroke.

dynamic characteristic in series mode. In parallel mode, the step response time is 0.101 s as shown in figure 26(b). There is a certain improvement compared with the series mode.

6.2. The repeatability of the pump

The repeatability of the pump directly determines the stability of the DPEHA output. Therefore, a series of tests were carried out to evaluate the repeatability of the pump employed in the DPEHA. The output displacement curves of DPEHA under different voltages are shown in figure 27(a), and the out capacity of the piezoelectric pump in the process is shown in figure 27(b). Which indicated that the output displacement of DPEHA is stable under different driven voltages, and the output capacity of the piezoelectric pump fluctuates in the initial stage but gradually converges and tends to be stable. The piezoelectric pump employed in this paper has a good repeatability.

7. Conclusions

In this work, a piezoelectric material-based DMEHA is proposed for the application of the next generation of more electric aircraft. Mathematical modeling and parameter identification are conducted and presented. Experiments based on a fabricated prototype are carried out to investigate its characteristics. Conclusions can be made as

(a) The DMEHA configuration provides an alternative framework for designing smart material-based multi-pump EHAs.
(b) The established mathematical model has good agreement with experimental results in terms of dynamic and static characteristics. This provides useful guidance for designers and researchers.
(c) The serial-parallel hybrid working mode can be realized by the DMEHA for the adaptability of different

actuation requirements. This takes both the advantages of the multi-pump serial structure and the multi-pump parallel structure.

(d) Experimental results show that the DMEHA has a maximum output flow of 1.17 $1\,min^{-1}$ at 360 Hz under the serial mode and a blocking load of up to 40 kg. The corresponding maximum output flow in the parallel mode can reach 1.97 $1\,min^{-1}$ at 420 Hz, and the blocking load is 20 kg.

Future work will seek to control algorithm design for the actuator to improve the tracking accuracy and dynamic response properties.

Data availability statement

No new data were created or analysed in this study.

Acknowledgment

This work was supported by the National Natural Science Foundation of China (Grant Number 51975275), the National Key Laboratory of Science and Technology on Helicopter Transmission (Grant No. HTL-A-22G03), the Primary Research & Development Plan of Jiangsu Province (Grant No.BE2021034), and the Fundamental Research Funds for the Central Universities (Grant No. NS2022051).

ORCID iDs

Jie Ling https://orcid.org/0000-0002-6786-0422
Long Chen https://orcid.org/0000-0002-2565-5631
Yuchuan Zhu https://orcid.org/0000-0002-7399-1656

References

[1] Gohardani A S, Doulgeris G and Singh R 2011 *Prog. Aerosp. Sci.* **47** 369–91
[2] Jiao Z, Zhang H, Shang Y, Liu X and Wu S 2020 *Aerosp. Sci. Technol.* **106** 106177
[3] Sarlioglu B and Morris C T 2015 *IEEE Trans. Transp. Electrification* **1** 54–64
[4] Buticchi G, Bozhko S, Liserre M, Wheeler P and Al-Haddad K 2018 *IEEE Trans. Ind. Electron.* **66** 5588–99
[5] Huang L, Yu T, Jiao Z and Li Y 2020 *Appl. Sci.* **10** 6978
[6] Yan W, Shengrong G and Hongkang D 2020 *Chin. J. Aeronaut.* **33** 365–71
[7] Sakaino S and Tsuji T 2017 *IFAC-PapersOnLine* **50** 12065–70
[8] Li Y and Jiao Z 2016 *Chin. J. Mech. Eng.* **52** 37–37
[9] Kumar M 2021 *Mater. Today: Proc.* **45** 6057–63
[10] Chao Q, Zhang J, Xu B, Huang H and Pan M 2019 *J. Mech. Des.* **141** 050801
[11] Alle N, Hiremath S S, Makaram S, Subramaniam K and Talukdar A 2016 *Int. J. Fluid Power* **17** 125–45
[12] Guo Y, Zhu Y, Li Y, Fei S, Zhu B, Zhang X and Wang X 2018 *J. Intell. Mater. Syst. Struct.* **29** 1348–59
[13] Zhu Y, Wang Z and Fei S 2019 *Proc. Inst. Mech. Eng.* I **233** 994–1008
[14] Wang R, Zhu Y, Jiang Y and Chen L 2020 *Smart Mater. Struct.* **29** 035003
[15] Chaudhuri A and Wereley N 2012 *J. Intell. Mater. Syst. Struct.* **23** 597–634
[16] Wax S, Fischer G and Sands R 2003 *JOM* **55** 17–23
[17] Yang X, Zhu Y and Zhu Y 2018 *Proc. Inst. Mech. Eng.* G **232** 847–60
[18] Li Y, Jiao Z and Wang Z 2020 *Sensors* **20** 634
[19] Zhu Y, Yang X and Wereley N M 2016 *Smart Mater. Struct.* **25** 085030
[20] Zhu Y and Li Y 2014 *Smart Mater. Struct.* **23** 115001
[21] Chen L, Zhu Y, Ling J and Zhang M 2022 *IEEE/ASME Trans. Mechatronics* **27** 2071–9
[22] Bartlett P, Eaton S, Gore J, Metheringham W and Jenner A 2001 *Sens. Actuators* A **91** 133–6
[23] Qin Y, Shirinzadeh B, Tian Y, Zhang D and Bhagat U 2013 *IEEE/ASME Trans. Mechatronics* **19** 872–81
[24] Yang Z, He Z, Li D, Cui X, Xue G and Zhao Z 2015 *Sensors Actuators* A **236** 228–46
[25] Tian Y, Lu K, Wang F, Zhou C, Ma Y, Jing X, Yang C and Zhang D 2020 *IEEE/ASME Trans. Mechatronics* **25** 1322–34
[26] Chen L, Zhu Y, Ling J and Feng Z 2021 *IEEE/ASME Trans. Mechatronics* **26** 1951–9
[27] Wu Y, Liu Y, Liu J, Wang L, Jiao X and Yang Z 2013 *J. Mech. Sci. Technol.* **27** 793–8
[28] Wang J, Liu Y, Shen Y, Chen S and Yang Z 2016 *Micromachines* **7** 219
[29] Pan Q, Jiang H, Li Y, Wang Q, Huang B, Li R and Feng Z 2020 *Int. J. - Acoust. Vib.* **25** 549–55
[30] Pan Q, Li Y, Diao W, Wang X, Zhang C, Liu S and Li R 2022 *Smart Mater. Struct.* **31** 065023
[31] Ullmann A 1998 *Sens. Actuators* A **69** 97–105
[32] Kan J, Tang K, Liu G, Zhu G and Shao C 2008 *Sens. Actuators* A **144** 321–7
[33] Dong J S *et al* 2017 *Microsyst. Technol.* **23** 3019–26
[34] Wang Z, Zhu Y, Li R, Liu C and Bruno N 2019 *J. Intell. Mater. Syst. Struct.* **30** 1871–81
[35] Zhu Y, Liu C, Song Y, Chen L, Jiang Y and Wu C 2022 *J. Intell. Mater. Syst. Struct.* **33** 330–41
[36] Yao J, Jiao Z and Ma D 2014 *IEEE Trans. Ind. Electron.* **61** 6285–93
[37] Li Y, Le V T, Goo N S, Kim T H and Lee C S 2017 *J. Intell. Mater. Syst. Struct.* **28** 2557–71
[38] Woo J, Sohn D K and Ko H S 2019 *J. Mech. Sci. Technol.* **33** 661–7